



Development of zinc oxide-based sub-micro pillar arrays for on-site capture and DNA detection of foodborne pathogen

Kwang Se Lee^{a,1}, Younseong Song^{a,1}, Chi Hyun Kim^a, Yong Tae Kim^b, Taejoon Kang^c, Seok Jae Lee^e, Bong Gill Choi^{d,*}, Kyoung G. Lee^{a,*}

^aNanobio Application Team, National NanoFab Center (NNFC), Daejeon 34141, Republic of Korea

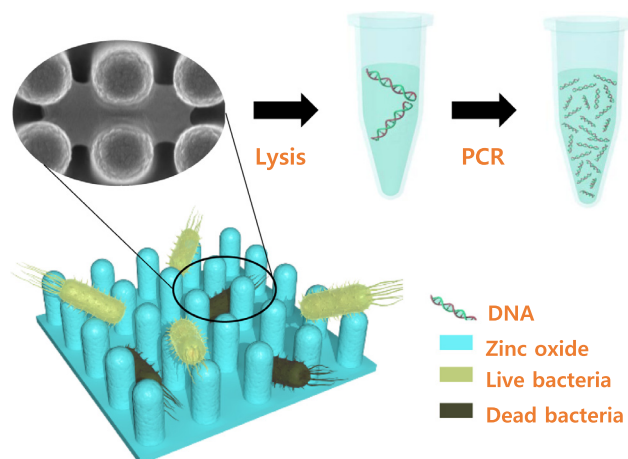
^bDepartment of Chemical Engineering & Biotechnology, Korea Polytechnic University, 237 Sangidaehak-ro, Siheung-si, Gyeonggi-do 15073, Republic of Korea

^cBionanotechnology Research Center, Korea Research Institute of Bioscience & Biotechnology, Daejeon 34141, Republic of Korea

^dDepartment of Chemical Engineering, Kangwon National University, Samcheok 25913, Republic of Korea

^eNanobio Application Team, National NanoFab Center (NNFC), 291 Daehak-ro, Yuseong-gu, Daejeon 305-701, Republic of Korea

GRAPHICAL ABSTRACT



ARTICLE INFO

Article history:

Received 3 October 2019

Revised 30 November 2019

Accepted 2 December 2019

Available online 14 December 2019

Keywords:

Pillar arrays
Bacteria capture
Foodborne pathogen
Genetic analysis
Zinc oxide

ABSTRACT

Prevention and early detection of bacterial infection caused by foodborne pathogens are the most important task to human society. Although currently available diagnostic technologies have been developed and designed for detection of specific pathogens, suitable capturing tools for the pathogens are rarely studied. In this paper, a new methodology is developed and proposed to realize effective capturing through touchable flexible zinc oxide-based sub-micro pillar arrays through genetic analysis. Zinc oxide coated pillar arrays have a high surface area, flexible, and adheres strongly to bacteria. Therefore, it contributes to enhance the bacterial capturability. An in-depth analysis on the sub-sequential capturing process at the bacterial cell-pillar interface is presented. By carefully observing the structural changes and performing numerical analysis under different reaction times, the results are presented. The resulting zinc oxide coated pillar arrays exhibited comprehensive capturability. These pillars were able to detect pathogenic bacteria due to a combination of complex structures, depletion force, and high surface

* Corresponding authors.

E-mail addresses: bgchoi@kangwon.ac.kr (B.G. Choi), kglee@nnfc.re.kr (K.G. Lee).

¹ These authors contributed equally.

electrostatics. The developed sub-micro pillars successfully captured and detected infectious foodborne bacteria of *Escherichia coli* in the range of 10^6 – 10^1 CFU/mL.

© 2019 Elsevier Inc. All rights reserved.

1. Introduction

Effective capture and detection of infectious pathogenic bacteria is great of importance in the field of diagnostics, therapeutics, and healthcare [1–5]. In particular, the rapidly growing numbers of foodborne illnesses around the world, such as food poisoning, has lead researchers to focus on the prevention of pre- and post-contamination from potential foodborne bacteria [4,6–8]. Bacterial foodborne pathogens commonly exist on the surface of kitchenware, silverware, as well as raw food materials. This is due to the continuous exposure to inadequate hygienic facilities and inadequate sanitation practices. Even though progresses have been made in the detection and analysis of pathogenic bacteria using both immunoassays and molecular diagnostics, effective capturing tools are rarely developed and the capturing mechanisms are not understood. Therefore, to manage food safety, on-site, cost-effective, sensitive, and reliable capturing tools via touching are highly demanded.

Up-to-date, antibody-based immunoassay with zero- and one-dimensional (0D and 1D) organic and/or inorganic nanomaterials that includes carbon dots [9,10], silica [11,12], magnetic particles [12,13], and nanowires [14] have been widely adopted to bind with pathogenic bacteria. However, non-specific binding issues, low adhesiveness, low stability of antibodies, and complex steps to fabricate nanomaterials with target specificity hinder application in real life [15,16]. A promising approach is to utilize interaction between topological structures of nanomaterials and the surface of bacteria [5,17–20]. As an example, Linklater et al. enhanced the interaction between vertically-aligned carbon nanotubes and bacterial cells to realize bactericidal properties [19]. In addition, Liu et al. proposed to upgrade the performance of the bacterial capturability in fluid bloodstreams by controlling mechanical properties and nano-topological interactivity of inorganic nanowires [17]. Liu et al. showed that polycrystalline nanowires with numerous grain boundaries exhibit excellent mechanical bending properties when compared to single crystals that resulted in higher bacterial capturability. Likewise, various types of inorganic nanostructures have been researched and among them, zinc oxide (ZnO)-based nanomaterials have received a lot of attention due to its potential of interactivity with various kinds of biomolecules, including protein, deoxyribonucleic acid (DNA), mammalian cells, and bacteria [21–24]. Furthermore, ZnO-based nanomaterials have exhibited good biocompatibility, non-toxicity, and significant antibacterial activity [25–28]. Although the ZnO proves its capability, the low stiffness, brittleness, and strong agglomeration of ZnO-based nanoparticles and wires are still major hurdle to be used as bacterial capturing tool [29]. More importantly, the nanotopological interactivity between the surface of ZnO-based materials and pathogenic bacteria is rarely investigated which could be a key to enhance its capturability.

To overcome the challenges mentioned in the paragraph above and to adopt the mechanical and chemical characteristics of the avo-mentioned inorganic materials, recent advances in nanotechnology and nanofabrication techniques with polymers have allowed the fabrication of vertical nanopillar arrays [30–32]. These approaches support mechanical stability and flexibility that can be served as a unique platform for adherent mammalian cells, microorganisms, and biomolecules through nano-topological interactions [33,34]. Inspiring from previous findings, herein, we

report the novel method to capture and detect pathogenic bacteria using ZnO with a wrinkled surface and introduce positive surface charge and topological effects leading to interaction of negatively charged bacteria. The sub-micro pillar arrays (PAs) are fabricated by photo/soft-lithography process to have a 700 nm diameter and it is gold sputtered by the sonochemical method to ensure even growth. During this process the time-dependent interactivity between pathogenic bacteria and ZnO-coated PAs (Z-PAs) are investigated to determine the nano-topological interactions. Finally, it is confirmed that Z-PAs has the capability to capture and detect bacteria by genetic analysis with the assistance of polymerase chain reaction (PCR) amplification.

2. Experimental section

2.1. Materials.

2.1.1. Preparation of Z-PAs

Sub-micron PAs that included polyurethane acrylate (MINS-311RM, Minuta Technology) and Norland Optical Adhesive 63 (NOA 63, Norland Products Inc.) were fabricated by a combined photo/soft-lithography process used in [30]. The PAs were coated with a thin layer of titanium/gold by a sputtering process within a vacuum. Afterwards, the PAs were placed in the mixture of 0.01 M zinc acetate dihydrate ($\text{Zn}(\text{CH}_3\text{COO})_2 \cdot 2\text{H}_2\text{O}$, 98%, Sigma-Aldrich) and 1.57 M ammonia water ($\text{NH}_3 \cdot 2\text{H}_2\text{O}$, 28 wt%, Sigma-Aldrich) and sonicated for 30 min for the deposition of thin ZnO layer. Z-PAs arrays were rinsed several times with ethanol (CH_3OH , 99.8%, Sigma-Aldrich) and deionized water and dried under a vacuum after the sonication reaction has taken place.

2.1.2. Characterization

The sub-micron PAs and bacteria captured images were observed using a field emission scanning electron microscope (SEM) (S-4800, Hitachi) equipped with an X-ray spectrometer for elemental mapping. The spectrum was analyzed with a Fourier transform infrared spectroscopy (FT-IR) Bruker IFS 66v/S spectrometer coupled with a Hyperion 3000 infrared (IR) microscope. X-ray diffraction patterns were measured on a Rigaku D/MAX-2500 diffractometer with Cu-KR radiation ($\lambda = 1.5418 \text{ \AA}$). X-ray photoelectron spectroscopy (XPS) analysis was performed on a Thermo VG Scientific Sigma Probe spectrometer. Focused ion beam (FIB) (FB-2100, Hitachi) allows cross-sectional observations. The roughness of the NP arrays, Z-PAs, and the bacteria were captured and the Z-PAs were measured using an atomic force microscope (AFM) (AFM XE100, Park Systems). The zeta potential of the ZnO particles was calculated from the electrophoretic mobilities measured (ELS-Z2, Otsuka).

2.1.3. Cell preparation

E. coli O157:H7 was used as the foodborne pathogens and was grown separately in a 15 mL tube that contained an LB medium and was incubated with overnight shaking (250 rpm) at a temperature of 37 °C. The cell density was quantified by UV absorption at 600 nm and the initial optical density (OD) was 1.0, a value that is equivalent to 10^9 cells/mL.

2.1.4. Preparation of PCR reagents and amplification

As a realistic foodborne pathogen model, *E. coli* O157:H7 was selected and incubated overnight in a 15 mL tube containing LB medium, shaking vigorously (150 rpm) at 37 °C. The cell density was further quantified by UV absorption at 600 nm and the initial OD was 1.0 which is equivalent of 10^9 cells/ml. The genomic sequence of *E. coli* O157:H7 was obtained from GenBank and the *eaeA* gene of *E. coli* O157:H7 was selected as the target gene. The forward primer is 5'-GAC CCG GCA CAA GCA TAA GC-3', and the reverse primer is 5'-CCA CCT GCA GCA ACA AGA GG-3'. The amplicon size of this target gene was 384 bp.

The extracted genomic DNA (gDNA) from *E. coli* O157:H7 was mixed in a PCR cocktail, including the dNTP, MgSO₄, forward and reverse primer, and Taq polymerase. The PCR was conducted under the following incubations: 300 sec of pre-denaturation at 95 °C, 30 sec of denaturation of 95 °C, 30 sec of annealing at 60 °C, 30 sec of extension of 72 °C. During the last cycle, the extension time was extended to 300 sec with a C1000 Touch™ Thermal Cycler (Bio-rad). Real-time PCR (RT-PCR) was also carried out using 20X SFC green I dye (BioFACT, Korea). Each reaction contained 25 µL of the following ingredients: 1.25 µL of 20X SFC green I dye, 2 µL each of forward and reverse primer (10 µM), 1 µL of template DNA, and 18.75 µL of the PCR reaction cocktail (Promega). RT-PCR was conducted using a Magnetic Induction Cycler (Biomolecular system). The thermal cycling conditions were as follows: 95 °C for 5 min (initial denaturation and thermal lysis of cell), 40 cycles of 95 °C for 30 sec, 60 °C for 30 sec, 72 °C for 30 sec, and the final extension was at 72 °C for 5 min.

3. Results and discussion

The schematic illustration for the design and preparation of PA, gold-coated PAs (G-PAs), and ZnO-coated G-PAs (Z-PAs) and its bacterial capturing processes is shown in Fig. 1a. The usage of polymeric PAs enables us to deposit ZnO on the surface and to offer both high surface areas as well as effective capturing. The polymeric PAs were prepared by photo- and soft-lithography as previously reported [30].

The surface morphology of PAs, G-PAs, Z-PAs, and after exposing Z-PAs to bacteria were observed by SEM as shown in Fig. 1b–e. SEM images of each step revealed PAs with a diameter of 500 nm and height of 1.2 µm with a smooth surface (Fig. 1b). The roughness of the PAs increased slightly after the gold was deposited, but the most of the PAs were relatively equal when compared to the pristine PAs (Fig. 1c). After formation, the thin ZnO layer on the PAs exhibited almost no structural deformation, even after being exposed to the ultrasonication processes. The overall diameter and height of PAs (500 nm, 1.2 µm), G-PAs (600 nm, 1.3 µm), and Z-PAs (700 nm, 1.4 µm) were gradually increased after deposition of Ag and ZnO, respectively. Additionally, no visible cracks or damages were observed even after harsh bending. This confirmed that Z-PAs exhibits excellent flexibility and mechanical stability (Fig. S1). Furthermore, the SEM images of the bent Z-PAs also supported the negligible structural variations from external stress.

To investigate the proper coating of PAs with ZnO, a cross-sectional image of Z-PAs was prepared and further carried out for element mapping (Fig. 2a). The different elements of Zn, O, and Au were observed only along the surface of the PAs due to the uniform coating of both the Au and ZnO. Additionally, element mapping of Z-PAs also confirmed the sonochemical method enabled formation of ZnO over the surface of G-PAs in a short reaction time (<10 min).

Fig. 2b shows the chemical composition of the surface layers of PAs, Z-PAs, and B@Z-PAs using FT-IR spectroscopy. The typical

band (at approximately 3000 cm⁻¹) derived from C–H stretching vibrations is commonly observed from the polyurethane acrylate backbone of PAs. The peaks of polyurethane acrylate at 1730 cm⁻¹, 1683 cm⁻¹, 1458 cm⁻¹, 1140 cm⁻¹, and 765 cm⁻¹ were attributed to the presence of C=O stretching, CH₃ bending, N–H bending, and C–N stretching, respectively. From the FT-IR spectrum of Z-PAs, the peaks at 623 cm⁻¹ corresponds to Zn–O stretching and deformation vibration. The peaks at 1440 cm⁻¹ and 1700 cm⁻¹ are mainly attributed to C–H and hydroxyl groups, respectively [35]. Interestingly, the main peaks from PAs disappeared because of the ZnO coating on the surface. From the FT-IR spectrum of B@Z-PAs, four distinctive spectra regions were observed and are defined as follows: (1) 900–700 cm⁻¹ is the “fingerprint region” which indicates discrimination and/or identification purposes of bacteria, (2) the region between 1200 and 900 cm⁻¹ is the absorption band of carbohydrates in microbial walls, also known as the polysaccharide region, (3) the 1700–1500 cm⁻¹ region contains the amide I and II bands of proteins and peptides, and (4) the region of 3000–2800 cm⁻¹ is the fatty acid region [36]. These unique FT-IR peaks, especially in the region of 900–700 cm⁻¹ is approximately comparable to previously reported *E. coli* O157:H7. Thereby, the FT-IR results strongly supported the successful deposition of ZnO on the PAs and successful capture of target bacteria on the Z-PAs surface.

To further investigate the ZnO formation on the PAs, an XPS analysis was carried out as shown in Fig. 2c. The XPS graph of pristine polyurethane-based PAs showed the presence of oxygen, nitrogen, and carbon from the binding energy peaks at 534, 401, and 286 eV. After the coating of ZnO on the PAs, the distinctive binding energy peak at 1025 eV corresponded to the Zn_{2p₃} [37]. Thereby, subsequent analysis using XPS indicated the presence of Zn atoms, further confirming the formation of the ZnO on the PAs (Fig. 2c).

The bacterial interaction mechanism is important in order to optimize structural design and it is essential to understand how the topologies of regular PAs influence bacteria capture. Hence, we hypothesized that the behavior of bacteria interaction with Z-PAs would differ under varying reaction times. Based on this hypothesis, Fig. 3a demonstrates the bacteria capturing processes after dropping. As expected, the morphology of the bacteria continuously changed under varying reaction times, and SEM images of the top views revealed these phenomena (Fig. 3b–e). To get a better indication of bacteria capture, enlarged cross-sectional SEM images are also presented in Fig. 3f–i. The pristine Z-PAs showed repeatable PAs with aspect ratio (1:2, 700 nm/1.4 µm). As soon as the bacteria solution was dropped onto the Z-PAs surface, *E. coli* O157:H7 cells immediately interacted with Z-PAs and some of these cells were sitting slightly in-between the pillars (Fig. 3c). However, there were minor structural changes of Z-PAs when compared to the pristine Z-PA at the early stage of contact. By increasing the reaction time, the bacterial cell slowly penetrated into the pillars and the bacteria cell formed a cellular bridge in-between the Z-PAs (Fig. 3c, d, g, and h). It followed that the cell was finally touched the surface of Z-PA substrate (Fig. 3e and i). These series of bacterial interaction phenomena is occurred the combination of cell interaction with PAs at early stage and slowly moved down to the surface because of complex depletion force generation in between cells and PAs. Moreover, the deformation of both the bacterial cell and the pillars were observed from the cross-sectional SEM images as shown in Fig. 3f–i.

This attraction phenomena can be also defined from the well-known binding and depletion force of either bacteria-to-bacteria or bacteria-to-material surface. The positively-charged surface (zeta potential, ζ approximately 20 mV) from ZG and nanotopology of PAs could contribute to strong adhesion of bacterial cells on the surface, either by binding or by a depletion attraction (Fig. S2)

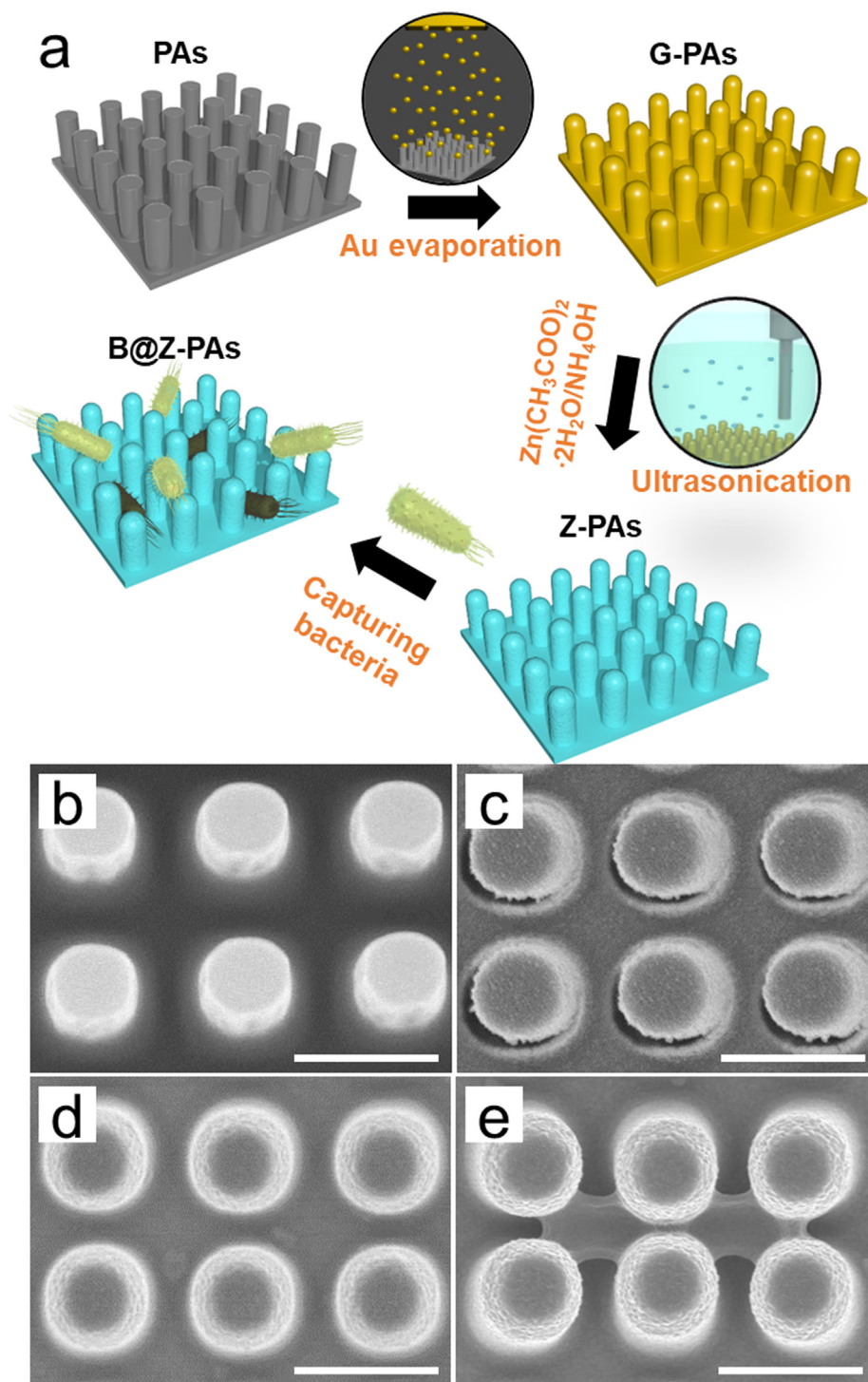


Fig. 1. (a) Schematic illustration of the fabrication procedures of the Z-PAs for capturing bacteria. SEM images of (b) PAs, (c) G-PAs, (d) Z-PAs, (e) B@Z-PAs. Scale bars in (d–e) are 1 μm .

[38]. Additionally, common secretion of extracellular polymeric substances (EPSs), which are mostly composed of polysaccharides and proteins, is another key parameter that leads to spontaneous adhesion [39]. As a result of these complex depletion and binding forces, the pillar tilts toward the contact direction with bacteria and the tilt angles of the pillars can be clearly observed in the side view presented in Fig. 3h. The bacterium was deeply embedded beneath the pillar, disappeared, and trapped inside of the Z-PAs due to the out-focusing of the SEM as shown in Fig. 3e and i.

To better understand this phenomenon, an in-depth analysis of displacement distance and tilt angles of the individual pillars after interaction with the bacterium is determined by measuring of the pillar position along the x- and y-axis (Fig. S3). The detailed schematic illustration of side view and top view of both pristine Z-PAs and B@Z-PAs are shown in Fig. 3j. In the side view, the height (h) of the pillar is shown as approximately 1400 nm and the distance between the center to the pillar before and after the bacteria is captured are marked as d and d' , respectively, where φ is the tilting

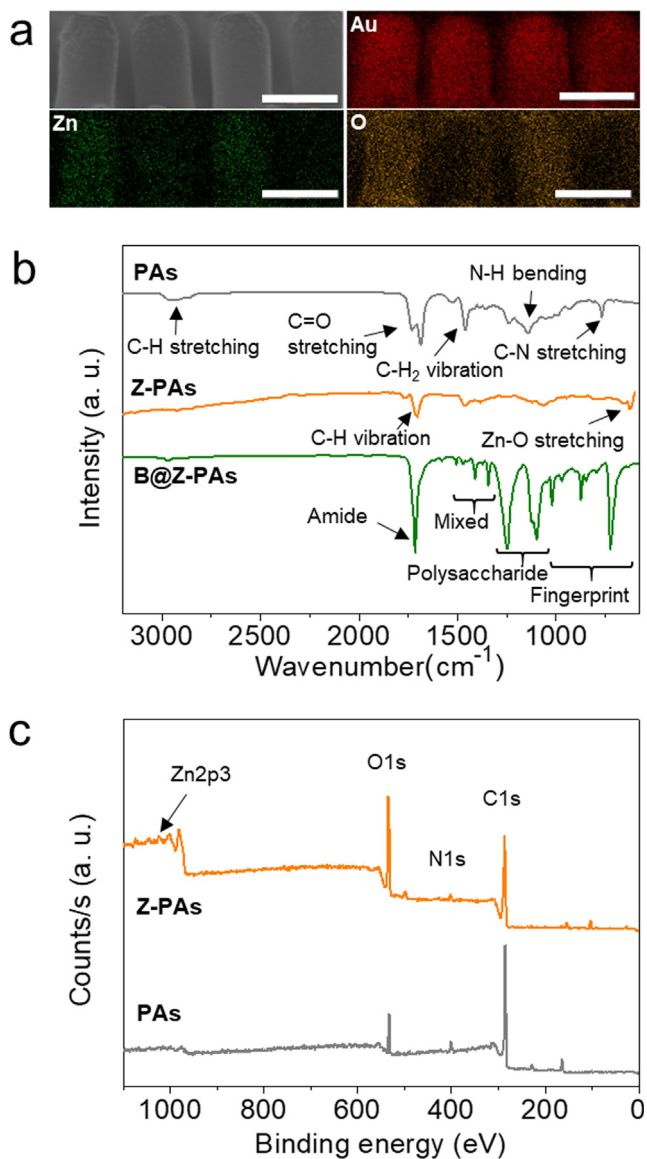


Fig. 2. (a) SEM images of Z-PAs and the corresponding elemental mapping images of Zn, O, and Au, respectively. Scale bars in (a) is 1 μm . (b) FT-IR spectra of PAs, Z-PAs and B@Z-PAs. (c) Survey scan of XPS spectra of PAs and Z-PAs.

angle. To simplify the analysis on deformation, orthogonal, and diagonal displacements are chosen as the standard displacement motion in the top view. The pristine orthogonal and diagonal distances (d_o , d_d) are approximately 500 nm and 700 nm, respectively. The tilting angle is obtained through numerical analysis on the orthogonal and diagonal distances of the tilted pillar relative to the original. The equation used to determine the tilt angle is given as: $\varphi = \tan^{-1} \left\{ \frac{d-d'}{h} \right\}$.

Due to the different bacterial positions from the top to the bottom, the displacement distance was varied from 28.1 nm to 123.2 nm for the orthogonal direction and from 25.1 nm to 103.3 nm for the diagonal direction. The results indicated that the orthogonal displacement was higher than that of the diagonal displacement due to the higher contact surface with the bacterium. Additionally, the tilting angle of the pillar was maximized to average 5.0° and 4.2° toward the orthogonal and the diagonal direction, respectively, when the bacterium is totally touched to the bottom.

To investigate the capture capabilities and detection limits, *E. coli* O157:H7 bacteria cells were 10-fold diluted from 10⁶ to 10¹ CFU/mL and spread over the Z-PAs. The SEM images revealed the small size of the black rods (the bacteria) located in-between Z-PAs (Fig. 4a-f). The SEM images also revealed that the amount of captured bacteria is dependent on the concentration of the cell. It was also found that all the bacteria were closely surrounded and also interacted with *at least* six pillars. Consequently, Z-PAs show an excellent ability to immobilize pathogenic bacteria and the gradual increasing the amount of black rods from the SEM images also confirmed its performance. Through this work, this unique bacterial capture ability of Z-PAs could therefore be attributed to two aspects: (1) Z-PA carries more bacteria to the surface because of a large surface area and a strong positively-charged surface, and (2) the flexibility and optimized pocket size leads to an increase in interactivity between Z-PA and bacteria.

To validate the capture and detection capabilities of Z-PA, specific genetic analysis was applied and the detailed processes of bacterial lysis, gene extraction, and amplification are demonstrated in Figs. 4g and S4. To ensure that effective bacteria capturability of the Z-PAs, RT-PCR was carried out with targeting the *eaeA* gene of *E. coli* O157:H7. In this work, we compared the RT-PCR results from a gDNA of the target bacteria that was extracted using the conventional method and the RT-PCR results from a gDNA that was extracted using Z-PAs captured bacteria cells. The resulting cycle threshold (Ct) values is plotted in Fig. 4h. The Ct values from the B@Z-PAs were slightly lower than the conventionally extracted gDNA due to the loss of the target cells during the capturing. Even through the additional bacteria capturing process, the Ct values were relatively similar to the control samples, meaning our method had an excellent bacteria capturability. As a result, the surface of the Z-PAs could effectively capture pathogenic *E. coli* O157:H7 cells, the gDNAs were also recoverable from the bacteria after being immobilized on the Z-PAs surface.

Finally, after important consideration for on-site capture and detection of foodborne pathogens, we carefully selected representative food and silverware items of egg and spoon representing silverware in daily life. The egg and spoon were artificially infected with *E. coli* O157:H7 and the surfaces of both items were rubbed using the Z-PAs films (Fig. 4i). The gDNAs were carefully extracted and amplified with PCR and Fig. 4j shows electrophoresis gel images after these amplifications. We observed the resultant signals from both the egg and the spoon, which indicated the successful recovery of bacteria and the amplification of target genes from *E. coli* O157:H7. From this experiment, we can confirm that the Z-PAs can be used for on-site foodborne pathogens isolation and it is applicable to identifying pathogens incorporated in PCR amplification.

4. Conclusions

This work proposes advanced inorganic-organic hybrid nanocomposite PAs through combination of photo- and soft-lithography, with the assistance of ultrasound irradiation. The unique hybrid composite PAs showed a strong antibacterial property through complex topological interaction between the bacteria and the ZnO surface of sub-micron PAs. In addition, ultrasound irradiation allowed us to fabricate uniform ZnO-coated pillars in short reaction time (<10 min) without showing significant structural damage or aggregation. The Z-PAs revealed a good hydrophilicity and a positively-charged surface that enhance the bacterial capturing capability. Compared to other inorganic-based bacterial capturing, this work focuses on spontaneous immobilization and interaction processes of a single bacterium among PAs. Moreover, the movement among the PAs under different interac-

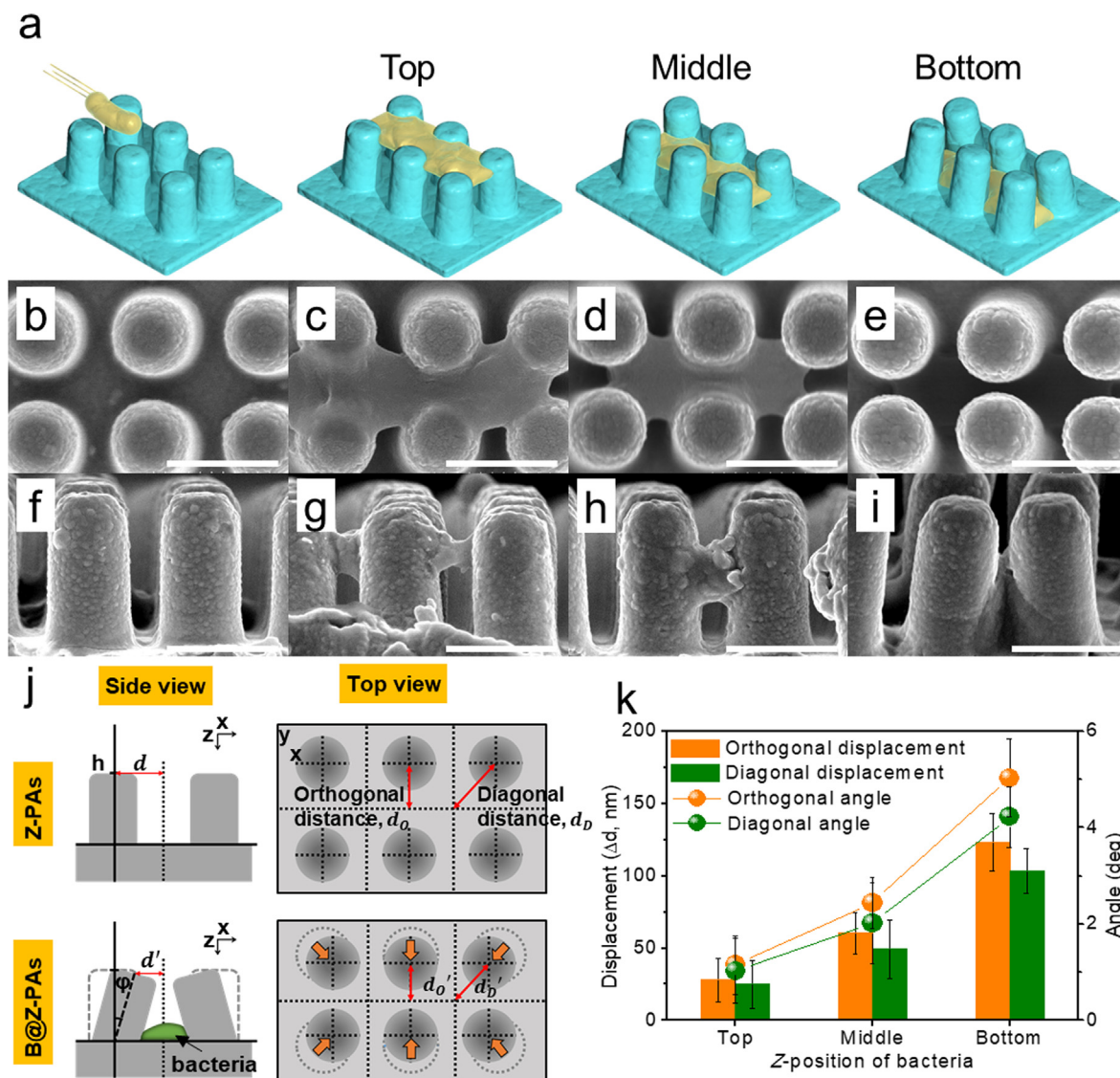


Fig. 3. (a) Schematic illustration of captured bacteria positioning on Z-PAs and the corresponding SEM images: (b–e) top view and (f–i) side view, respectively. Scale bars in (b–i) are 1 μm . (j) Geometry parameters for a tilted Z-PA and B@Z-PAs depicting a tilting angle (ϕ), orthogonal displacement (d_o - d_o') and diagonal displacement (d_d - d_d') when a bacterium is captured on a nanopillar array. (k) Relationship between the bacteria position on the nanopillar array and the lateral deflection (x -displacement and tilting angle). The displacement (Δd , nm) and angle (degree) is calculated by $n = 20$ for each position.

tion time successfully demonstrated how the sub-micron structures, electrostatic attraction, and depletion forces spontaneously interact at the bacterial cell-to-pillar interface. From the SEM investigation, the structural deformation of PAs and formation of bacterial bridges in-between PAs, both orthogonal and diagonal displacement along with bending of PAs affected in all the x , y , and z axis because of bacteria provided unique features and enhancement of bacteria capturability. To the best of our knowledge, this is the first case where depletion and topology-induced spontaneous aggregation of bacterial cells and pillars are performed. Consequently, as a result of excellent and robust capture performance of Z-PAs, it allowed us to detect pathogenic bacteria in the range of 10^6 to 10^8 CFU/mL by extraction of DNA and its amplification. Moreover, the direct bacterial capturing and detection performance also confirmed that from daily used food items (i.e. egg) and silverware (i.e. spoon). Additionally, the excellent capturing performance enabled us to deploy this Z-PAs film to recover pathogenic bacteria from real life usage items. Thereby,

our approach could eventually be extended to apply this to realize on-site detection of pathogens.

CRediT authorship contribution statement

Kwang Se Lee: Conceptualization, Methodology, Investigation, Writing - original draft. **Younseong Song:** Conceptualization, Methodology, Writing - original draft, Visualization. **Chi Hyun Kim:** Investigation. **Yong Tae Kim:** Investigation. **Taejoon Kang:** Resources. **Seok Jae Lee:** Resources. **Bong Gill Choi:** Conceptualization, Writing - review & editing, Supervision. **Kyoung G. Lee:** Conceptualization, Writing - review & editing, Supervision.

Declaration of Competing Interest

The authors declare that they have no known competing financial interests or personal relationships that could have appeared to influence the work reported in this paper.

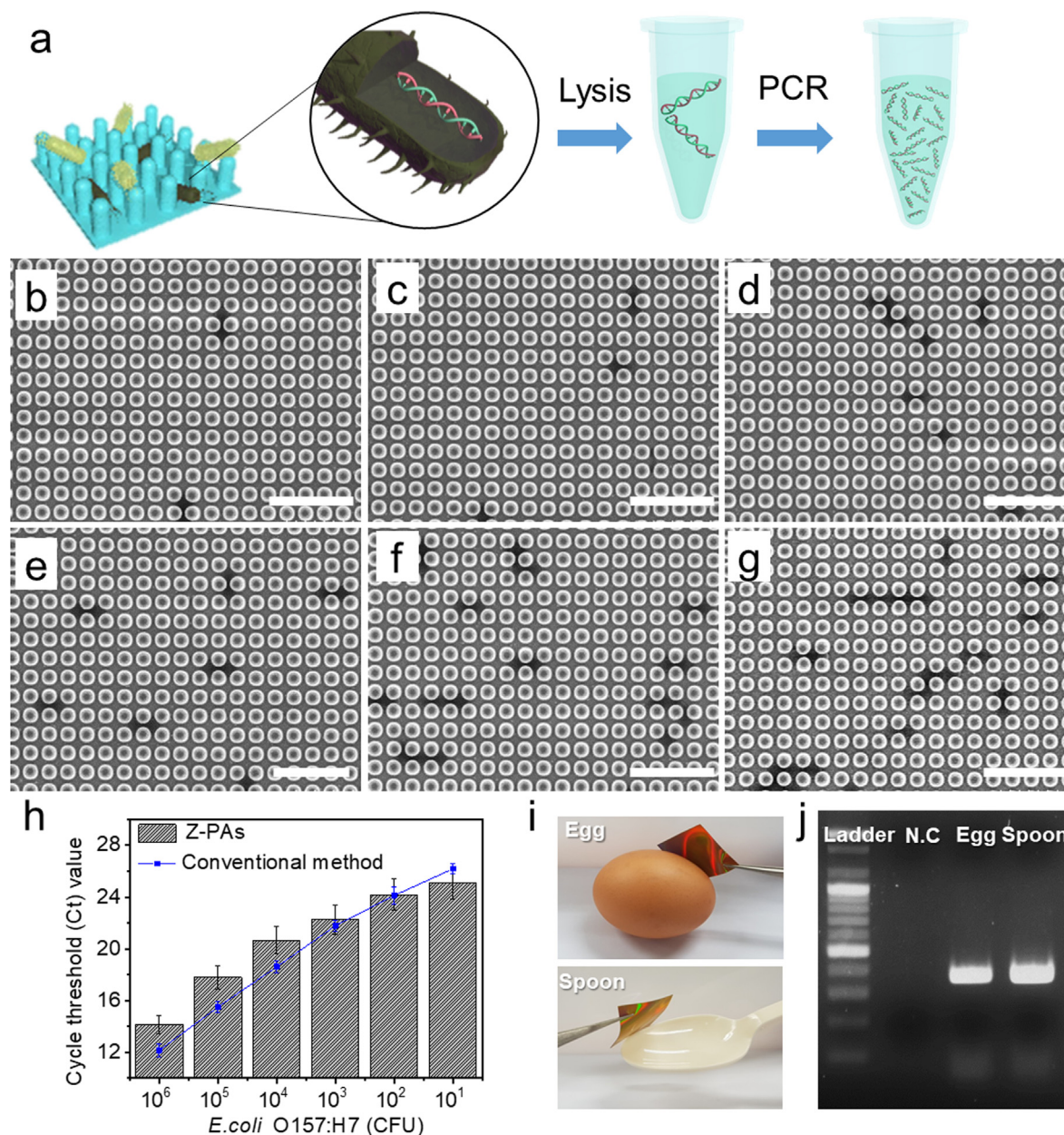


Fig. 4. SEM images of B@ZNP arrays at bacteria concentration of (a) 10, (b) 10², (c) 10³, (d) 10⁴, (e) 10⁵, and (f) 10⁶ CFU/ml. All the scale bars are 5 μ m. (g) Bacterial lysis and PCR amplification processes of B@Z-PAs. (h) Ct values, the mean \pm standard deviation ($n = 3$), from RT-PCR of *E. coli* O157:H7 comparing the B@Z-PAs and the conventional method in a range of 10⁶ to 10¹ CFU. (i) Photographic images of real sample test using artificially infected egg and a spoon with Z-PAs and (j) the corresponding agarose gel electrophoresis results of PCR amplifications.

Acknowledgement

The authors contributed equally in this work. This research was supported by Basic Science Research Program through the National Research Foundation of Korea (NRF) and funded by the Ministry of Science, ICT & Future Planning (2018R1C1B3001553). This research was also supported by BioNano Health-Guard Research Center funded by the Ministry of Science and ICT (MSIT) of Korea as Global Frontier Project (Grant number H-GUARD_2014M3A6 B2060302 and H-GUARD_2013M3A6B2078950). This work was supported by the Nano Material Technology Development Program through the National Research Foundation of Korea funded by the Ministry of Science and ICT (No. 2017M3A7B4039936). This work is also supported by Nano Open Innovation Lab Cooperation Project of NNFC and KRIBB Research initiative Program.

Appendix A. Supplementary material

Supplementary data to this article can be found online at <https://doi.org/10.1016/j.jcis.2019.12.008>.

References

- [1] L. Varadi, J.L. Luo, D.E. Hibbs, J.D. Perry, R.J. Anderson, S. Orenge, P.W. Groundwater, Methods for the detection and identification of pathogenic bacteria: past, present, and future, *Chem. Soc. Rev.* 46 (2017) 4818–4832.
- [2] D. Ivnitski, I. Abdel-Hamid, P. Atanasov, E. Wilkins, Biosensors for detection of pathogenic bacteria, *Biosens. Bioelectron.* 14 (1999) 599–624.
- [3] L. Yang, R. Bashir, Electrical/electrochemical impedance for rapid detection of foodborne pathogenic bacteria, *Biotechnol. Adv.* 26 (2008) 135–150.
- [4] K.S. Gracias, J.L. McKillip, A review of conventional detection and enumeration methods for pathogenic bacteria in food, *Can. J. Microbio.* 50 (2004) 883–890.

- [5] W. Kim, J.K. Ng, M.E. Kunitake, B.R. Conklin, P. Yang, Interfacing silicon nanowires with mammalian cells, *J. Am. Chem. Soc.* 129 (2007) 7228–7229.
- [6] B. Swaminathan, P. Feng, Rapid detection of food-borne pathogenic bacteria, *Annu. Rev. Microbiol.* 48 (1994) 401–426.
- [7] Y. Choi, Y.T. Kim, J.B. You, S.H. Jo, S.J. Lee, S.G. Im, K.G. Lee, An efficient isolation of foodborne pathogen using surface-modified porous sponge, *Food Chem.* 270 (2019) 445–451.
- [8] Y.M. Park, S.Y. Lim, S.J. Shin, C.H. Kim, S.W. Jeong, S.Y. Shin, N.H. Bae, S.J. Lee, J. Na, G.Y. Jung, A film-based integrated chip for gene amplification and electrochemical detection of pathogens causing foodborne illnesses, *Anal. Chim. Acta* 1027 (2018) 57–66.
- [9] L. Yang, W. Deng, C. Cheng, Y. Tan, Q. Xie, S. Yao, Fluorescent immunoassay for the detection of pathogenic bacteria at the single-cell level using carbon dots-encapsulated breakable organosilica nanocapsule as labels, *ACS Appl. Mater. Inter.* 10 (2018) 3441–3448.
- [10] Y. Lin, Q. Zhou, D. Tang, R. Niessner, D. Knopp, Signal-on photoelectrochemical immunoassay for aflatoxin B1 based on enzymatic product-etching MnO₂ nanosheets for dissociation of carbon dots, *Anal. Chem.* 89 (2017) 5637–5645.
- [11] C. Zhu, G. Zhao, W. Dou, Core-shell red silica nanoparticles based immunochromatographic assay for detection of *Escherichia coli* O157: H7, *Anal. Chim. Acta* 1038 (2018) 97–104.
- [12] J.-L. Gong, Y. Liang, Y. Huang, J.-W. Chen, J.-H. Jiang, G.-L. Shen, R.-Q. Yu, Ag/SiO₂ core-shell nanoparticle-based surface-enhanced Raman probes for immunoassay of cancer marker using silica-coated magnetic nanoparticles as separation tools, *Biosens. Bioelectron.* 22 (2007) 1501–1507.
- [13] J. Hu, Y.-Z. Jiang, M. Tang, L.-L. Wu, H.-Y. Xie, Z.-L. Zhang, D.-W. Pang, Colorimetric-fluorescent-magnetic nanosphere-based multimodal assay platform for salmonella detection, *Anal. Chem.* 91 (2018) 1178–1184.
- [14] Z. Guo, Y. Jia, X. Song, J. Lu, X. Lu, B. Liu, J. Han, Y. Huang, J. Zhang, T. Chen, Giant gold nanowire vesicle-based colorimetric and sers dual-mode immunosensor for ultrasensitive detection of vibrio parahaemolyticus, *Anal. Chem.* 90 (2018) 6124–6130.
- [15] E. Wujcik, H. Wei, X. Zhang, J. Guo, X. Yan, N. Sutrave, S. Wei, Z. Guo, Antibody nanosensors: a detailed review, *RSC Adv.* 4 (2014) 43725–43745.
- [16] B. Byrne, E. Stack, N. Gilmartin, R. O’Kennedy, Antibody-based sensors: principles, problems and potential for detection of pathogens and associated toxins, *Sensors* 9 (2009) 4407–4445.
- [17] L. Liu, S. Chen, Z. Xue, Z. Zhang, X. Qiao, Z. Nie, D. Han, J. Wang, T. Wang, Bacterial capture efficiency in fluid bloodstream improved by bendable nanowires, *Nat. Commun.* 9 (2018) 444.
- [18] J. Hasan, S. Jain, R. Padmarajan, S. Purighalla, V.K. Sambandamurthy, K. Chatterjee, Multi-scale surface topography to minimize adherence and viability of nosocomial drug-resistant bacteria, *Mater. Des.* 140 (2018) 332–344.
- [19] D.P. Linklater, M. De Volder, V.A. Baulin, M. Werner, S. Jessl, M. Golozar, L. Maggini, S. Rubanov, E. Hanssen, S. Juodkazis, High aspect ratio nanostructures kill bacteria via storage and release of mechanical energy, *ACS Nano* 12 (2018) 6657–6667.
- [20] S. Qi, C. Yi, S. Ji, C.-C. Fong, M. Yang, Cell adhesion and spreading behavior on vertically aligned silicon nanowire arrays, *ACS Appl. Mater. Inter.* 1 (2008) 30–34.
- [21] A. Sirelkhatim, S. Mahmud, A. Seeni, N.H.M. Kaus, L.C. Ann, S.K.M. Bakhori, H. Hasan, D. Mohamad, Review on zinc oxide nanoparticles: antibacterial activity and toxicity mechanism, *Nano-Micro Lett.* 7 (2015) 219–242.
- [22] L. Wang, Q. Zhao, Z. Zhang, Z. Lu, Y. Zhao, Y. Tang, Fluorescent conjugated polymer/quarternary ammonium salt Co-assembly nanoparticles: Applications in highly effective antibacteria and bioimaging, *ACS Appl. Bio Mater.* 1 (2018) 1478–1486.
- [23] N. Tripathy, D. Kim, Metal oxide modified ZnO nanomaterials for biosensor applications, *Nano Convergence* 5 (2018) 27.
- [24] G. Patrinoiu, R. Dumitru, D.C. Culita, C. Munteanu, R. Birijega, J.M. Calderon-Monreno, A. Cucos, D. Pelinescu, M.C. Chifriuc, C. Bleotu, O. Carp, Self-assembled zinc oxide hierarchical structures with enhanced antibacterial properties from stacked chain-like zinc oxalate compounds, *J. Colloid Interf. Sci.* 885 (2019) 258–270.
- [25] Q. Cai, Y. Gao, T. Gao, S. Lan, O. Simalou, X. Zhou, Y. Zhang, C. Harnooode, G. Gao, A. Dong, Insight into biological effects of zinc oxide nanoflowers on bacteria: why morphology matters, *ACS Appl. Mater. Inter.* 8 (2016) 10109–10120.
- [26] Y. Zhu, X. Liu, K.W. Yeung, P.K. Chu, S. Wu, Biofunctionalization of carbon nanotubes/chitosan hybrids on Ti implants by atom layer deposited ZnO nanostructures, *Appl. Surf. Sci.* 400 (2017) 14–23.
- [27] C. Mao, Y. Xiang, X. Liu, Z. Cui, X. Yang, K.W.K. Yeung, H. Pan, X. Wang, P.K. Chu, S. Wu, Photo-inspired antibacterial activity and wound healing acceleration by hydrogel embedded with Ag/Ag@ AgCl/ZnO nanostructures, *ACS Nano* 11 (2017) 9010–9021.
- [28] M. Banik, P. Chakrabarty, A. Das, S.K. Ray, R. Mukherjee, Colloidal transfer printing-mediated fabrication of zinc oxide nanorods for self-cleaning applications, *Adv. Mater. Interf.* 6 (2019) 1900063.
- [29] S.-W. Bian, I.A. Mudunkotuwa, T. Rupasinghe, V.H. Grassian, Aggregation and dissolution of 4 nm ZnO nanoparticles in aqueous environments: influence of pH, ionic strength, size, and adsorption of humic acid, *Langmuir* 27 (2011) 6059–6068.
- [30] K.G. Lee, B.G. Choi, B.I. Kim, T. Shyu, M.S. Oh, S.G. Im, S.J. Chang, T.J. Lee, N.A. Kotov, S.J. Lee, Scalable nanopillar arrays with layer-by-layer patterned overt and covert images, *Adv. Mater.* 26 (2014) 6119–6124.
- [31] Y. Zhang, C.-W. Lo, J.A. Taylor, S. Yang, Replica molding of high-aspect-ratio polymeric nanopillar arrays with high fidelity, *Langmuir* 22 (2006) 8595–8601.
- [32] M.K. Choi, H. Yoon, K. Lee, K. Shin, Simple fabrication of asymmetric high-aspect-ratio polymer nanopillars by reusable AAO templates, *Langmuir* 27 (2011) 2132–2137.
- [33] C. Xie, Z. Lin, L. Hanson, Y. Cui, B. Cui, Intracellular recording of action potentials by nanopillar electroporation, *Nat. Nanotechnol.* 7 (2012) 185.
- [34] L. Hanson, W. Zhao, H.-Y. Lou, Z.C. Lin, S.W. Lee, P. Chowdary, Y. Cui, B. Cui, Vertical nanopillars for in situ probing of nuclear mechanics in adherent cells, *Nat. Nanotechnol.* 10 (2015) 554.
- [35] M. Gharagozlu, S. Naghibi, Sensitization of ZnO nanoparticle by vitamin B12: Investigation of microstructure, FTIR and optical properties, *Mater. Res. Bull.* 84 (2016) 71–78.
- [36] C. Quintelas, E.C. Ferreira, J.A. Lopes, C. Sousa, An overview of the evolution of infrared spectroscopy applied to bacterial typing, *J. Biotechnol.* 13 (2018) 1700449.
- [37] H. Huang, P. Xu, D. Zheng, C. Chen, X. Li, Sulfuration–desulfuration reaction sensing effect of intrinsic ZnO nanowires for high-performance H₂S detection, *J. Mater. Chem. A* 3 (2015) 6330–6339.
- [38] D. Marenduzzo, K. Finan, P.R. Cook, The depletion attraction: an underappreciated force driving cellular organization, *J. Cell. Biol.* 175 (2006) 681–686.
- [39] B. Boury, S. Plumejeau, Metal oxides and polysaccharides: an efficient hybrid association for materials chemistry, *Green Chem.* 17 (2015) 72–88.